KEK Preprint 2004-97
February 2005
H

Σ^+p elastic scattering cross sections in the region of 350 $\leq P_{\Sigma^+} \leq$ 750 MeV/c with a scintillating fiber active target

KEK-PS E289 collaboration

J.K.Ahn [a], H. Akikawa [a], J. Arvieux [b], B. Bassalleck [c], M.S. Chung [a], H. En'yo [a], T. Fukuda [d], H. Funahashi [a], S.V. Golovkin [e], A.M. Gorin [e], Y. Goto [a], M. Hanabata [f], T. Hayakawa [g], A. Ichikawa [a], M. Ieiri [h], K. Imai [a], M. Ishino [a], H. Kanda [a], Y.D. Kim [i], Y. Kondo [a], E.N. Kozarenko [j], I.E. Kreslo [j], J.M. Lee [k], A. Masaike [a], S. Mihara [g], K. Nakai [g], K. Nakazawa [f], K. Ozawa [a], A. Sato [g], H.D. Sato [a], K.S. Sim [l], T. Tabaru [a], F. Takeutchi [m], P. Tlustý [d], H. Torii [a], K. Yamamoto [a], S. Yokkaichi [a] and M. Yoshida [a]

[a] *Department of Physics, Kyoto University, Kyoto 606-8502, Japan*
[b] *Laboratory National Saturne, F-91191, Gif-sur-Yvette, Ceder, France*
[c] *Department of Physics, University of New Mexico, NM 87131, U.S.A.*
[d] *Institute for Nuclear Study, University of Tokyo, Tanashi, Tokyo 188-0002, Japan*
[e] *Institute for High Energy Physics, RU-142284 Protvino, Russia*
[f] *Physics Department, Gifu University, Gifu 501-1193, Japan*
[g] *Department of Physics, Tokyo University of Science, Noda, Chiba 278-8510, Japan*
[h] *INPS, KEK, High Energy Accelerator Research Organization, Tsukuba 305-0801, Japan*
[i] *Physics Department, Seoul National University, Seoul 151-742, South Korea*
[j] *Joint Institute for Nuclear Research, RU-141980 Dubna, Russia*
[k] *Department of Physics, Yonsei University, Seoul 120-749, South Korea*
[l] *Department of Physics, Korea University, Seoul 136-701, South Korea*
[m] *Department of Physics, Kyoto Sangyo University, Kyoto 603-8555, Japan*

Submitted to Nucl. Phys. A

High Energy Accelerator Research Organization

High Energy Accelerator Research Organization (KEK), 2005

KEK Reports are available from:

Science Information and Library Services Division
High Energy Accelerator Research Organization (KEK)
1-1 Oho, Tsukuba-shi
Ibaraki-ken, 305-0801
JAPAN

Phone: +81-29-864-5137
Fax: +81-29-864-4604
E-mail: irdpub@mail.kek.jp
Internet: http://www.kek.jp

$\Sigma^+ p$ elastic scattering cross sections in the region of $350 \leq P_{\Sigma^+} \leq 750$ MeV/c with a scintillating fiber active target

KEK-PS E289 collaboration

J.K. Ahn [a,1], H. Akikawa [a,2], J. Arvieux [b,3], B. Bassalleck [c], M.S. Chung [a,4], H. En'yo [a,5], T. Fukuda [d,6], H. Funahashi [a], S.V. Golovkin [e], A.M. Gorin [e], Y. Goto [a,7], M. Hanabata [f], T. Hayakawa [g,8], A. Ichikawa [a,9], M. Ieiri [h], K. Imai [a], M. Ishino [a,10], H. Kanda [a,*,11], Y.D. Kim [i,12], Y. Kondo [a,2], E.N. Kozarenko [j], I.E. Kreslo [j,13], J.M. Lee [k,14], A. Masaike [a,15], S. Mihara [a,10], K. Nakai [g], K. Nakazawa [f], K. Ozawa [a,16], A. Sato [g,17], H.D. Sato [a], K.S. Sim [ℓ], T. Tabaru [a,7], F. Takeutchi [m], P. Tlustý [d,18], H. Torii [a,7], K. Yamamoto [a,19], S. Yokkaichi [a,5], and M. Yoshida [a,20]

[a] *Department of Physics, Kyoto University, Kyoto 606-8502,Japan*

[b] *Laboratory National Saturne, F-91191, Gif-sur-Yvette, Cedex, France*

[c] *Department of Physics, University of New Mexico, NM 87131, USA*

[d] *Institute for Nucler Study, University of Tokyo, Tanashi, Tokyo 188-0002, Japan*

[e] *Institute for High Energy Physics, RU-142284 Protvino, Russia*

[f] *Physics Department, Gifu University, Gifu 501-1193, Japan*

Preprint submitted to Nuclear Physics A *2 February 2005*

[g] *Department of Physics, Tokyo University of Science, Noda, Chiba 278-8510, Japan*

[h] *INPS, KEK, High Energy Accelerator Research Organization, Tsukuba 305-0801, Japan*

[i] *Physics Department, Seoul National University, Seoul 151-742, South Korea*

[j] *Joint Institute for Nuclear Research, RU-141980 Dubna, Russia*

[k] *Department of Physics, Yonsei University, Seoul 120-749, Korea*

[ℓ] *Department of Physics, Korea University, Seoul 136-701, Korea*

[m] *Department of Physics, Kyoto Sangyo University, Kyoto 603-8555, Japan*

Abstract

A hyperon-nucleon scattering experiment, KEK-PS E289, was carried out at the K2 beam line. We adopted a scintillating fiber active target as a hydrogen target for hyperon production and subsequent hyperon-nucleon scattering. We collected more data than in a previous experiment, KEK-PS E251. In this paper, the differential cross sections for $\Sigma^+ p$ elastic scattering in the incident momentum range from 350 MeV/c to 750 MeV/c are presented and compared with theoretical predictions from the Nijmegen group (Nijmegen Soft Core 97) and the Kyoto-Niigata group (RGM-FSS and fss2).

Key words: $\Sigma^+ p$ elastic scattering, Hyperon-nucleon interaction, Differential cross sections, Scintillating fiber active target

PACS: 13.75.Ev, 21.30.Cb, 25.80.Pw

* Corresponding author.
[1] Present address: Department of Physics, Pusan National University, Pusan 609-735, South Korea
[2] Present address: Japan Atomic Energy Research Institute, Tokai-mura, Ibaraki-ken 319-1195, Japan
[3] Present address: Institut de Physique Nucléaire, Université Paris-sud, F-91406 Orsay-Cedex, France.
[4] Present address: Department of Physics, Korea University, Seoul 136-701, South Korea
[5] Present address: RIKEN, Institute of Physical and Chemical Research, Wako, Saitama 351-0198, Japan.
[6] Present address: Osaka Electro-Communication University, Neyagawa, Osaka 572-8530, Japan.
[7] Present address: RIKEN BNL Research Center, Brookhaven National Laboratory, Upton, NY 11973-5000, USA
[8] Present address: Central Japan Railway Company, Meieki 1-1-4, Nakamura, Nagoya, Aichi 450-6101, Japan.
[9] Present address: INPS, KEK, High Energy Accelerator Research Organization, Tsukuba 305-0801, Japan.
[10] Present address: ICEPP, International Center for Elementary Particle Physics, University of Tokyo, Tokyo 113-0033, Japan.
[11] Physics Department, Graduate school of science, Tohoku University, Sendai 980-8578, Japan
[12] Present address: Physics Department, Sejong University, Seoul, 143-747, South Korea.
[13] Present address: Università "La Sapienza" and INFN, I-00185 Rome, ITALY
[14] Present address: Korea Research Institute of Standards and Science, Taejoen 305-600, South Korea.
[15] Present address: Washington Office, Japan Society for the Promotion of Science, Washington DC, 20006 USA

1 Introduction

The nuclear force has long been investigated both theoretically and experimentally. In the theoretical approach, Yukawa's pion exchange theory was the first to employ a meson as the propagator of force between two nucleons. It successfully explained some characteristics of the nuclear force. However, the one pion exchange potential (OPEP) was only valid in the range of $r \geq 2$ fm. A multi-pion exchange or an exchange of heavier mesons should be incorporated in a description of the nuclear force in the shorter range ($1 < r < 2$ fm). There also was some complicateness in describing the repulsive core in the shortest range ($r < 1$ fm). Many kinds of theoretical models have been developed to describe the nucleon-nucleon (NN) interactions over the whole range. The Nijmegen group developed one boson exchange (OBE) models that describe the NN interactions based on SU(3) symmetry and the phenomenological core potential. They developed two types of models with different descriptions of the repulsive core: one with a hard core [1] and the other with a soft core [2][3]. The Bonn-Jülich group developed a multi-meson exchange model [4]. They derived the core potential from the ω meson exchange. The Kyoto-Niigata group [5], the Tokyo group [6], and the Tübingen group [7] have developed models with

[16] Present address: CNS, School of Science, Tokyo University, Tokyo 113-0033, Japan.
[17] Present address: Dept. of Physics, Osaka University, Toyonaka City, Osaka 560-0043 JAPAN
[18] Present address: Nuclear Physics Institute of the Academy of Science, 250 68 Řež, Czech Republic.
[19] Present address: Department of Physics, Osaka City University, Osaka 558-8585, Japan.
[20] Present address: RIKEN Yokohama Institute, Yokohama 230-0045, Japan

a short-range term based on the quark-cluster model (QCM) using the resonating group method. In spite of the differences in describing the short-range force between the theoretical models, nearly 10^4 experimental data for NN scattering (compiled in references [8][9][10]) can be finely reproduced. This implies that the description of the short range force is still an open problem. As for YN scattering, sparse experimental data measured in the 1960's [11] have been reproduced by finely tuned theoretical models, while predictions for experimentally unobserved values vary model by model. Therefore, new data on the YN scattering will set new constraints on the theories and reveal the mechanism of the short-range force. Experimental investigations into the YN interaction have an impact not only on the view of the YN interaction, but also on the view of the NN interaction.

A shortage of experimental data of the YN scattering mainly comes from the difficulties of handling hyperons. Due to the short lifetime of hyperons ($\sim 10^{-10}$ sec), the handling of a low-energy hyperon beam and the detection of hyperons after scattering are impossible. As a trackable active target for hyperon production and its scattering, a liquid-hydrogen bubble chamber had been the best device for low-energy hyperon scatterings [11]. Recently, a scintillating fiber (SCIFI) active target system was developed to detect short-lived particles and their subsequent decays at KEK. The SCIFI target system consists of a stack of scintillating fibers and image intensifiers (II's) to view photon images from the SCIFI block. The experiment KEK-PS E251, which measured the $\Sigma^+ p$ scattering cross sections, took advantage of the fast timing response of the II's for event triggering from the spectrometer information to accumulate Σ^+ relevant images efficiently [12]. The SCIFI records triggered images as digitized data. After an event-building process, each image was an-

alyzed with spectrometer information. By using a π^+ beam of 1.64GeV/c, and the setting the triggers on (π^+, K^+) reactions, 11 Σ^+p elastic scattering events for the momentum region $300 \leq p_{\Sigma^+} \leq 600$ MeV/c were successfully collected. As the next step, we tuned the parameters of the SCIFI target system for a faster timing, a higher spatial resolution, and a larger fiducial volume [13]. From those refinements, we aimed at gaining more statistics for Σ^+p scattering events and the first measurement of Σ^-p and scattering cross sections with the SCIFI target system. We used a π^+ beam of 1.64 GeV/c and a π^- beam of 1.33 GeV/c for measuring the Σ^+p and Σ^-p elastic scattering cross sections, respectively. The cross sections for Σ^-p elastic scattering were already reported in our previous paper [14]. In this paper, we present the differential cross sections for Σ^+p elastic scattering in the incident momentum range between 350 MeV/c and 750 MeV/c. This momentum region exceeds that of the previous bubble-chamber experiments, and overlaps that of the result from the KEK-PS E251 experiment. We also present the momentum dependence of the cross sections.

2 Experiment

The experiment was carried out at the K2 beam line in the East Counter Hall at the KEK 12 GeV PS. The primary proton beam was focused on a $\phi 6 \times 60$ mmL platinum target to create a π^+ beam. A separated π^+ beam of 1.64 GeV/c was hit on the SCIFI active target [13] to produce Σ^+'s through the (π^+, K^+) reaction. Scattered particles, including K^+, were particle identified and momentum analyzed by the spectrometer. The produced Σ^+ traveled through the active target and might have scattered on the protons in it.

Charged particles relevant to the reaction chain were observed as 3-dimensional tracks inside the active target. A top view of the experimental apparatus is shown in Fig. 1.

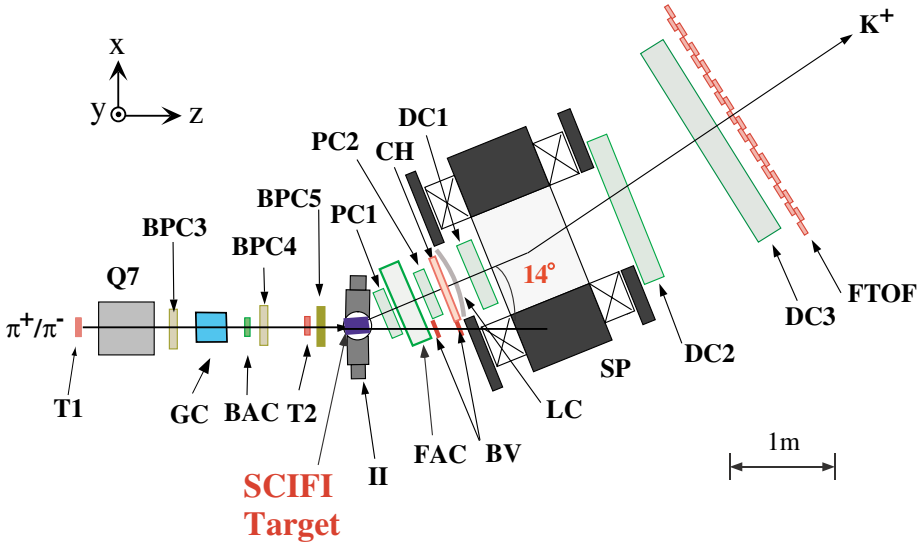

Fig. 1. Experimental setup for KEK-PS E289.

We used a π^+ beam of 1.64 GeV/c with a momentum bite of $\Delta p/p = 0.5$ % (RMS) and with an intensity of typically 2×10^5 per spill (extraction period of ~2 s in a cycle of 4 s). Particle identification was made by a gas Cherenkov counter (GC) and a beam-line aerogel Cherenkov counter (BAC). A radiator for GC was isobutane of 3 atm. It's radiation threshold was $\beta = 0.9989$, which was used for the ejection of positrons. A radiator for BAC was a block of newly developed hydrophobic aerogel [15], which had a refraction index of 1.042 to reject K^+'s and protons. A trigger according to the passage of a beam particle was issued by the coincidence of two plastic scintillation counters (T1 and T2) and BAC and a veto of GC. Time-of-flight information between T1 and T2 was also used for particle identification. Three multi-wire proportional chambers (BPC3, BPC4, and BPC5) were used to track the beam particles.

The spectrometer was placed downstream of the SCIFI active target. Its angular acceptance covered from 4 to 24 degrees in the laboratory system. We determined the position in consideration of both the forward peaking Σ^+ yield via the (π^+, K^+) reaction and the Σ^+ track recognition efficiency, which increased with the opening angle between the Σ^+ and K^+ tracks. The particle identification of K^+ was also done on-line and off-line. For the on-line first-level trigger, a Forward Aerogel Cherenkov counter (FAC) was used to reject pions, and a Lucite Cherenkov counter (LC) was used to reject protons. The sign of the particle charge was selected using a matrix coincidence of 2 sets of hodoscopes: Charge Hodoscope (CH) and Forward Time Of Flight counters (FTOF) before and after the spectrometer magnet, respectively. In the second-level trigger, we utilized a mass sensitive trigger system (Mass-Trigger) made of LeCroy ECLine logic modules to reduce proton contamination. It utilized combinations of the hits on CH and FTOF to obtain momentum information and TOF between T2 and FTOF for β information. From the matrix coincidence of the momentum and the β, it issued the second-level trigger for the K^+ mass region. The typical trigger rate was 10 to 20 per spill. In the off-line analysis, 3 multi-wire drift chambers (DC1, DC2, and DC3) and 2 multi-wire proportional chambers (PC1 and PC2) were used to track a charged particle in the magnetic field to measure its momentum. The momentum resolution ($\Delta p/p$) for a K^+ of 1.15 GeV/c was estimated to be less than 1.3% (RMS). The time-of-flight information between T2 and FTOF was used to measure the β of a particle with a resolution of $\Delta t \sim 140$ ps (RMS).

2.2 SCIFI active target

The SCIFI active target system [13] was used as a hydrogen target both for hyperon production and subsequent hyperon scattering on a proton. It was made from KURARAY SCSF-78 plastic scintillators of 300×300 μm^2 square cross section. Approximately 330 fibers of 30 cm long were arranged in parallel to create a 30 cm long and 10 cm wide "sheet". Around 600 sheets were stacked alternatively to the perpendicular directions to form a fiducial volume of $10 \times 10 \times 20$ cm^3. The ends of the sheets in two directions were bundled in 10×10 cm^2 cross sections and polished to be attached to image intensifier tubes (II's) with input windows of 10 cm diameter. Two aluminum evaporated PMMA plates were attached to the other ends of the bundled fiber sheets to increase the photon yield by reflection. In a test using a prototype fiber stack, attaching an aluminum evaporated mylar film increased the photon yield by 1.6 times and increased the effective attenuation length by 3 times. Two sets of II chain were used to view the scintillation photons from charged particles passing through scintillation fibers. They were set left(image-L) and right(image-R) of the beam line, respectively, for a v-z view and a u-z view (see Fig. 2). Each chain was made of two electrostatic type II's, one micro-channel plate (MCP) type II, a tapered fiber optic (FOP), and an electron bombarded CCD (EBCCD) for image intensification, image size reduction, image preservation before a trigger decision, a gating, and the digitization of a photon image. The details of the II chains are described elsewhere [13]. Digitized image data were stocked in a CAMAC memory module during the beam-extraction period and the stocked data were transferred to DAQ during the beam-acceleration period during a spill. The amount of memory was

256 kB, which could hold typically 20 images for a spill.

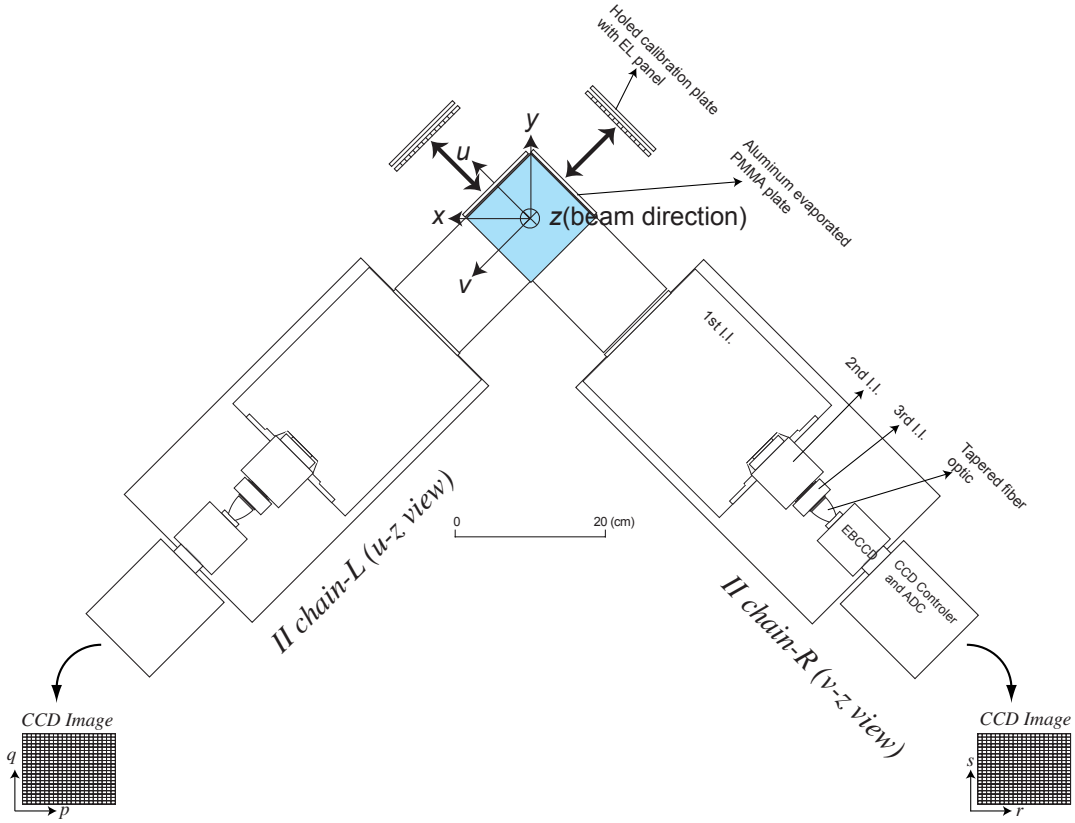

Fig. 2. Components of the II chains and their configuration. Two II chains were attached to view the projection to the u-z and v-z planes. CCD image coordinate systems are denoted as (p, q) and (r, s) for the u-z view and the v-z view, respectively.

2.3 Image compensation

Since there were an intrinsic distortion of the II's focusing lenses, the effect of a fringing magnetic field to the II's, the distortion of the FOP's and the deformation of stacked fibers, the image data suffered significant distortions. The distortions should be compensated so as to achieve sufficient tracking resolution. Image compensation means mapping the relation between CCD pixel coordinate system and the SCIFI local coordinate system: (u, v, z). The

locations in CCD pixel coordinates for image-L and image-R were denoted as (p, q) and (r, s), respectively (See Fig. 2). The mapping functions are described as follows:

$$\begin{aligned} u &= S_u(p, q), \\ z' &= S_{z'}(p, q), \\ v &= S_v(r, s), \\ z'' &= S_{z''}(r, s). \end{aligned}$$

We denoted the z-locations in image-L and image-R as z' and z'', because they should be different by the resolution of the image compensation. We obtained the z-location of the reconstructed 3-dimensional location by averaging z' and z''. We adopted the two dimensional B-spline for the mapping function $S(x, y)$, which was described as

$$S(x, y) = \sum_{i=1}^{h+m} \sum_{j=1}^{k+n} c_{ij} N_{mi}(x) N_{nj}(y),$$

where N_{mi} and N_{nj} are the i-th and j-th normalized B-spline functions of orders m and n for x and y directions, respectively. The number of knots for the x and y directions are denoted as h and k, respectively. Coefficients c_{ij} for each mapping function were obtained by the the 2-dimensional B-spline fitting (as known as the surface fitting) with grid points. We attached black PMMA plates with holes of ϕ1 mm aligned in a grid of 10 mm and 5 mm intervals in the z-direction and the direction perpendicular to the z-direction, respectively. Because the sizes in the z-direction were reduced by 2 times on the readout end of the SCIFI block, we obtained pictures of points aligned at equal intervals vertically and horizontally. For uniform illumination, electro-luminescence (EL) panels were put behind the holed plates. A sample of an obtained image of grid points for the u-z view is shown in Fig. 3(a). We made

a correspondence between the centroid of the i-th bright spot on the image (p_i, q_i) and the center position of the corresponding hole in real space (u_i, z_i). We obtained the mapping functions by minimizing the χ^2's, defined as follows:

$$\chi_u{}^2 = \sum_{n=1}^{N_{\rm cp}} (u_i - S_u(p_i, q_i))^2,$$
$$\chi_{z'}{}^2 = \sum_{n=1}^{N_{\rm cp}} (z_i - S_{z'}(p_i, q_i))^2,$$

where $N_{\rm cp}$ means the number of visible grid points. We adopted a group of netlib functions, DIERCKX[16], for fitting and evaluating the spline functions. In order to avoid the complexity of choosing spline knots, we used only additional knots that were the minimum and maximum ends of the CCD pixel coordinate. The quality of these fits was checked by the residual of the surface fitting. The RMS's of the residuals were typically 100 μm for the u and v directions and 170 μm for the z' and z'' directions. An image after compensation is shown in Fig. 3(b). The effectiveness of the compensation was demonstrated by the distributions of the line-fitting residuals for the minimum ionizing pion tracks before and after the compensation (Fig. 4). A typical compensated image data of a $\Sigma^+ p$ scattering is shown in Fig. 5.

3 Analysis

3.1 Spectrometer analysis to identify (π^+, K^+) reactions

During 420 hours of a data-taking shift, 3.1×10^6 triggers were issued. The momenta of charged particles and TOF between the T2 counter and the FTOF hodoscope were used to reconstruct the masses of the scattered particles passed

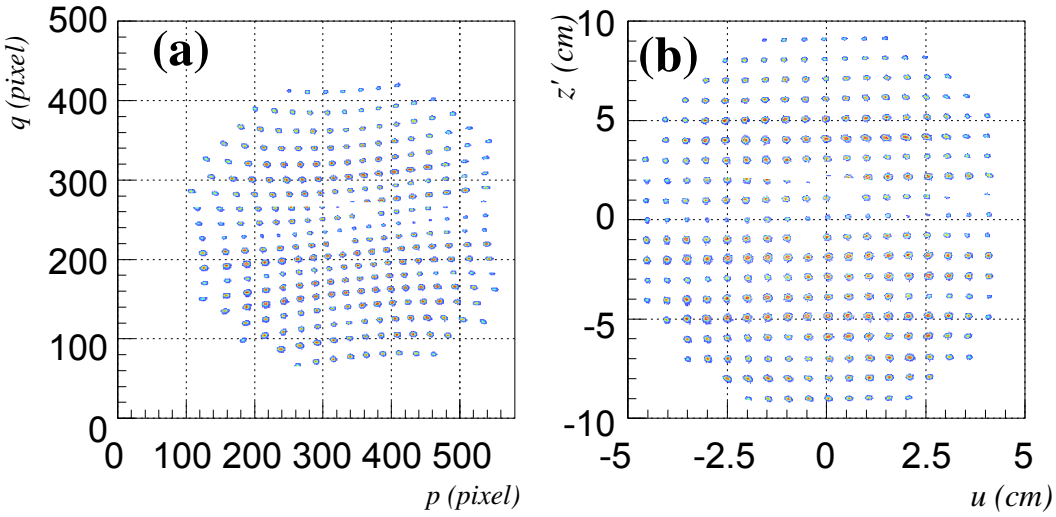

Fig. 3. Images of grid points of the II chain-L used to compensate of the image distortion. (a) Before compensation (in (p, q) coordinate); (b) After compensation (in (u, z') coordinate).

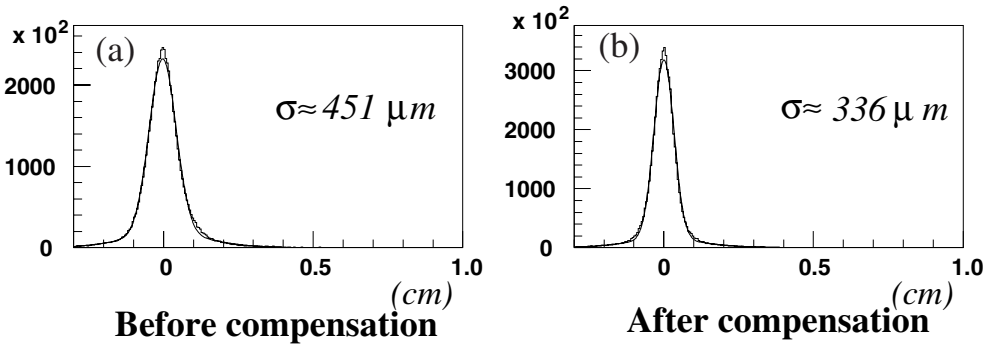

Fig. 4. Fitting residual distributions for straight tracks of the minimum ionizing pions. (a) Before image compensation; (b) After image compensation.

through the spectrometer. The mass spectra of the momentum-analyzed particles are shown in Fig. 6, which shows a mass resolution of $\Delta M = 24.8$ MeV/c^2 (RMS). By the spectrometer analysis, 1.3×10^6 (π^+, K^+) events were identified.

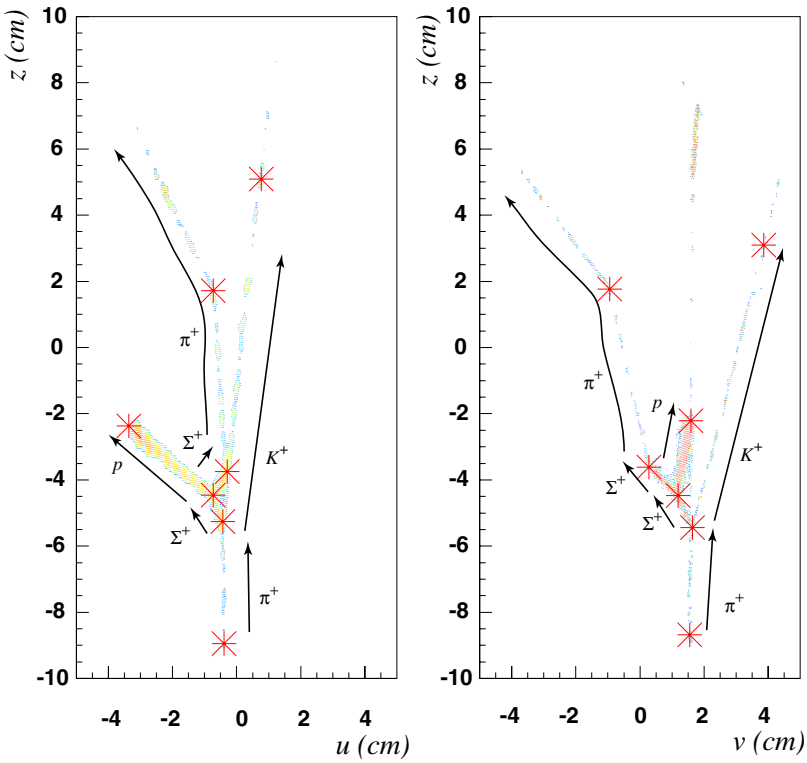

Fig. 5. Typical image data, which was identified as Σ^+p elastic scattering. (a) is for the u-z view; (b) is for the v-z view. In these pictures, stars represent the input positions in the pointing process described in section 3.2.

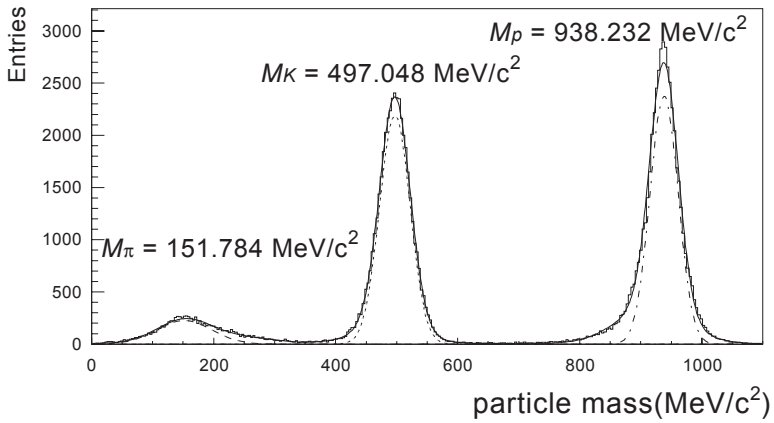

Fig. 6. Mass spectrum for the detected particles. Three peaks correspond to a pion, a kaon, and a proton, respectively. The fitted Gaussian functions are also shown.

3.2 Image analysis to identify Σ^+

Human scanners watched image data of (π^+, K^+) events on graphic terminals and categorized the events by track topologies. We called this process as "eye-

scanning". Roughly 30% of the (π^+, K^+) events were eye-scanned without any preprocessing (data set 1). The rest, 70% of the (π^+, K^+) events, underwent a cut by a computational image analysis before eye-scanning (data set 2) to shorten the eye-scanning period. The computational image analysis excluded events that did not contain thick bright tracks, which were expected to be Σ^+ tracks, along the direction of the missing momenta in the image data. The detailed description for the "thick" track can be found in Ref. [13]. By this process, 23.8% of the events were excluded. However, this process overkilled the true Σ^+ production events. To evaluate the overkilling ratio, a computational image analysis was performed to 2523 Σ^+ production candidates, categorized by physicists. Consequently, 2235 events survived the process. The overkilling ratio was estimated to be $11.4 \pm 0.6\%$. We called the efficiency of this process the image-tracking efficiency, $\epsilon_{\mathrm{itrack}} = 0.886 \pm 0.006$.

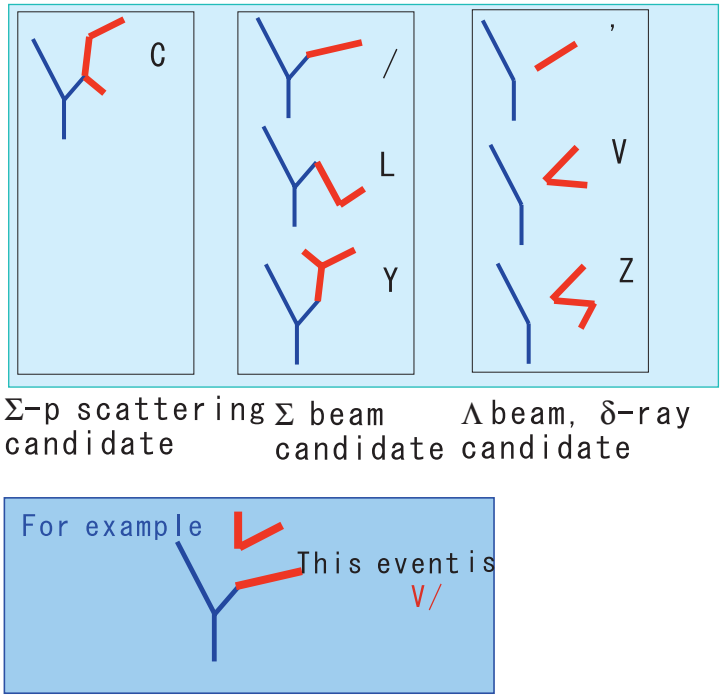

Fig. 7. Track patterns used for categorization in the eye-scanning.

Typical track topologies and signs for categorization are shown in Fig. 7. We

identified Σ^+ by its characteristic decay:

$$\begin{aligned}\pi^+ + p \rightarrow & \Sigma^+ + K^+ \\ & \hookrightarrow p + \pi^0(51.6\%), \\ & \hookrightarrow n + \pi^+(48.3\%).\end{aligned}$$

In both decays described above, thick tracks of Σ^+ have a kink at decay vertex in the image data. Images with one kink from a thick track were categorized as "/-type", and events with two or more kinks were categorized as "L-type." They were candidates for Σ^+ production events. Images that included Σ^+p scattering should show a more complex topology. That is, the thick track forks into two branches at the scattering vertex; then, one branch kinks at the decay vertex:

$$\begin{aligned}\Sigma^+ + p \rightarrow & \Sigma^+ + p \\ & \hookrightarrow p + \pi^0(51.6\%), \\ & \hookrightarrow n + \pi^+(48.3\%).\end{aligned}$$

Images with one kink after a branching were categorized as "C-type." They were candidates for Σ^+p scattering events. We have corrected 2.6×10^5 candidates for Σ^+ production events and 9361 candidates for Σ^+p scattering events. With the help of the scanners, we reconstructed the tracks of charged particles detected in the image data. The scanners watched images and input vertex positions and line segments in each track topology on graphic terminals. The input vertices were the Σ^+ production vertex and its decay vertex. The input line segments were the incoming π^+ track, the outgoing K^+ track, and the track of a decay product of Σ^+. For Σ^+p scattering candidates, one more vertex and one more line segment were input, that is the Σ^+p scattering vertex and the track of recoil proton. We call this process "pointing." All of the candidates for Σ^+p scattering and 1.0×10^4 candidates for Σ^+ production (sampling

ratio $\epsilon_{\rm sample}$ is 3.98%) underwent the re-confirmation of the categorization and the pointing process. Using these pointing data on each image as input parameters, χ^2 minimizing line-fitting for π^+ and K^+ tracks were performed to find the Σ^+ production vertex. However, a straight line fitting for Σ^+ tracks often failed because of its short and thick shape. Vectors of the produced and scattered Σ^+'s were calculated simply from the pointing data.

To estimate the analyzing efficiencies, Monte Carlo simulation data with image data were produced using GEANT 3.21 [17]. We added event generators for Σ^+ production reactions on both hydrogen and carbon nuclei, and for following Σ^+ scattering on hydrogen nuclei to the simulator package. The angular distribution of $p(\pi^+, K^+)\Sigma^+$ was taken from reference [18]. For the C$(\pi^+, K^+)\Sigma^+$X reaction, the Fermi motion of the target proton in a carbon nucleus was simulated to obtain the momentum distribution, given by following formula:

$$N(p) = \frac{N_0}{1 + exp(\frac{p({\rm GeV}/c) - 0.1}{0.05})}.$$

The angular distribution of $\Sigma^+ p$ elastic scattering was chosen to be isotropic. Image data were generated from the energy losses on each scintillating fiber. The brightness and spread of the tracks were calculated from the amount of energy loss. The distortion of the tracks was calculated from the imperfection of the fiber position and the alignment of fiber sheets and the simulated distortion of the II's. We tuned the following parameters to simulate the real image data:

- conversion factors from the energy deposit in a scintillating fiber to the number of photo-electrons at the 1st II,
- conversion factors from the number of photoelectrons to the height of the

bright spot on the CCD,

- amount of cross talk between fibers,
- spread of each single photo-electron image,
- non-linear spread of a bright image on the CCD.

In Figs. 8 and 9, the brightness distributions on each pixel and the brightness-weighted track widths (residual of the straight-line fitting) for simulated pion and proton tracks were compared to those in real track images. The brightness distributions and the track width for the simulated minimum ionizing pion tracks showed good similarity to the real data. The brightness distribution for the simulated proton tracks (Fig. 9(a')) were different from the real data. The difference came from the inadequacy of the simulation of the CCD mechanism. However, the shape of the track-width distribution and the σ value of the fitted Gaussian curve showed the good similarity. The generated images were randomly mixed in the data in order to let them undergo the same scanning and pointing process for estimating efficiencies, errors, and amount of background.

3.3 Amount of Σ^+ flux

Fig. 10 shows the recognition efficiencies as a function of the z position of Σ^+ production vertex, the Σ^+ track lengths, the track lengths of decay products (π^+ or p), and the angle between Σ^+ and its decay product. Choosing the regions where the recognition efficiencies are flat, the conditions for V_z (z position of Σ^+ production vertex) and $\theta_{\Sigma-\mathrm{DP}}$ (angle between a Σ^+ and a decay product track) were determined. We required l_Σ (length of a Σ^+ track before decay) to be longer than 0.5 cm for the flat recognition efficiency. The

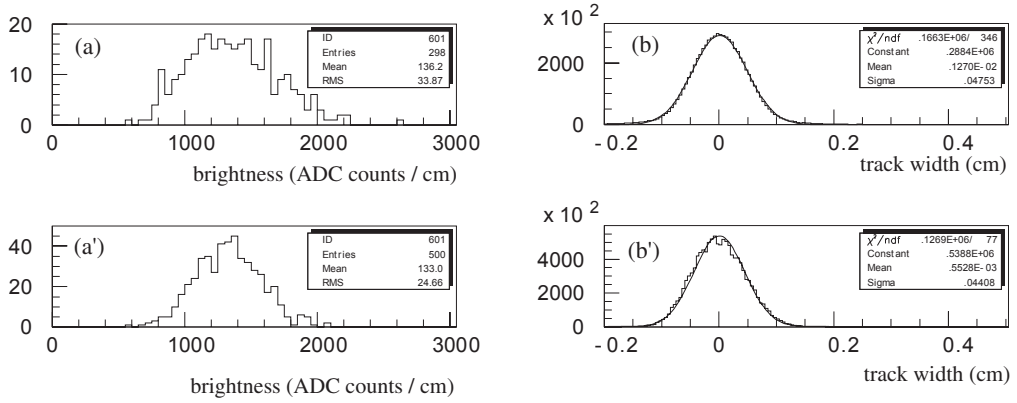

Fig. 8. Distributions of the pixel brightness per unit length (a) and the brightness weighted track widths (b) for the tracks of incident pions in the real image data. Corresponding figures (a') and (b') are for the minimum ionizing pion tracks in the simulated image data.

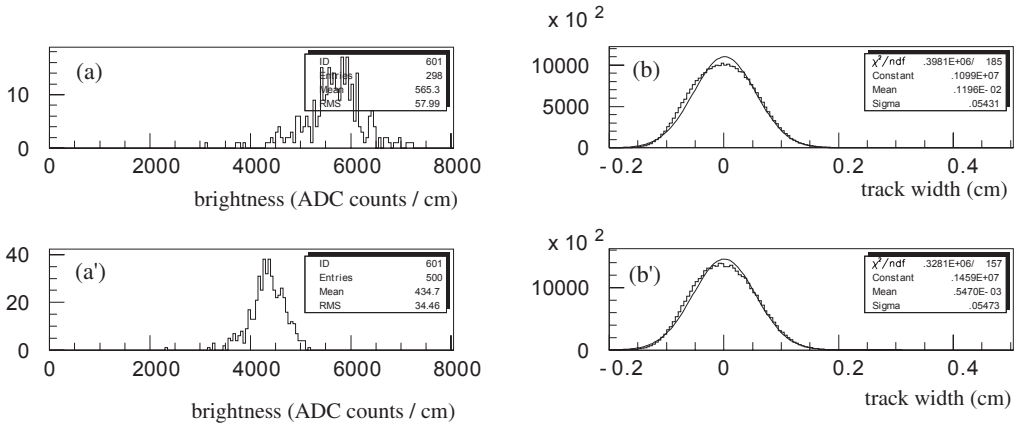

Fig. 9. Distribution of the pixel brightness per unit length (a) and the brightness weighted track widths (b) of the proton tracks with momenta of $p_p \sim 700$ MeV/c in the real image data. The corresponding figures (a') and (b') are for the proton tracks in the simulated image data.

maximum track length of Σ^+ was also set to be 5 cm. Since the probability to find a Σ^+ track longer than 5 cm was quite small in the simulation, the large length of the pointed Σ^+ track might be the result of misidentification. In summary, the visibility cut conditions for Σ^+ production events are as follows:

$$-9 \text{ cm} < V_z < 6 \text{ cm},$$

$0.5\ \mathrm{cm} < l_\Sigma < 5\ \mathrm{cm}$,
$\theta_{\Sigma-\mathrm{DP}} > 0.1$ rad.

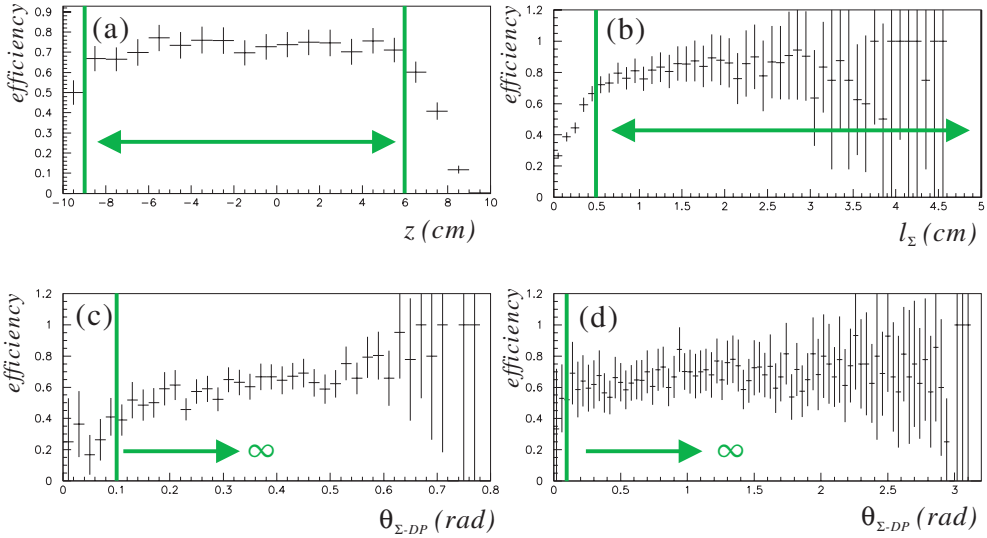

Fig. 10. Efficiencies in the eye-scanning process for simulated Σ^+ production events. (a) shows the dependence on the z position of the (π^+, K^+) vertex. (b) shows the dependence on the produced Σ^+ track length. The dependences on angle between a Σ^+ track and a charged track of decay products are shown in (c) the $p + \pi^0$ decay mode and (d) the $n + \pi^+$ decay mode. The arrows in the figure represent the selected region.

We also required the Σ^+ to be produced on the hydrogen nucleus. For selection, we set a requirement on the $p(\pi^+, K^+)$ missing mass (M_{miss}) and the angle between the $p(\pi^+, K^+)$ missing momentum and the pointed Σ^+ track ($\Delta\theta_\Sigma$). We defined $\Delta\theta_\Sigma$ as

$$\Delta\theta_\Sigma = \arccos\left(\frac{\vec{p}_{\mathrm{miss}} \cdot \vec{v}_\Sigma}{|\vec{p}_{\mathrm{miss}}||\vec{v}_\Sigma|}\right),$$

where $\vec{p}_{\mathrm{miss}}$ is the kinematically calculated vector for the $p(\pi^+, K^+)$ missing momentum, and $\vec{v}_\Sigma$ is the measured direction of Σ^+ obtained from the pointing process.

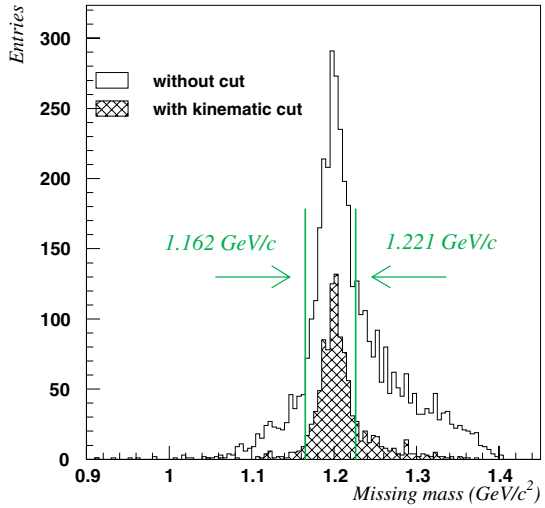

Fig. 11. Missing-mass spectrum for the $p(\pi^+, K^+)$ reaction. The hatched histogram shows events after the cut on $\Delta\theta_\Sigma$. The momentum region between two lines was selected as a Σ^+ beam produced on a hydrogen nucleus.

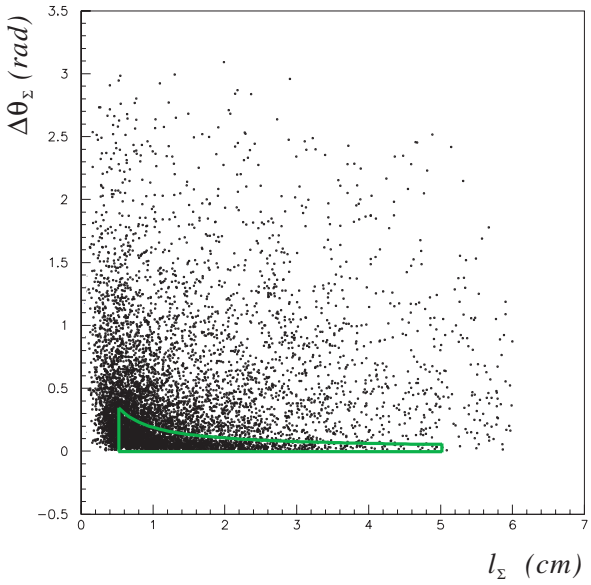

Fig. 12. Scatter plot of the angular difference between the (π^+, K^+) missing momentum vector and the pointed Σ^+ track vector vs. the length of pointed Σ^+ track. The area surrounded by the curve shows the selected region.

Fig. 11 shows the missing mass spectrum and the selected region. Fig. 12 shows the scattering plot of $\Delta\theta_\Sigma$ vs l_Σ. Because the angular resolution of pointed Σ^+ track strongly depends on the Σ^+ track length, cut region of

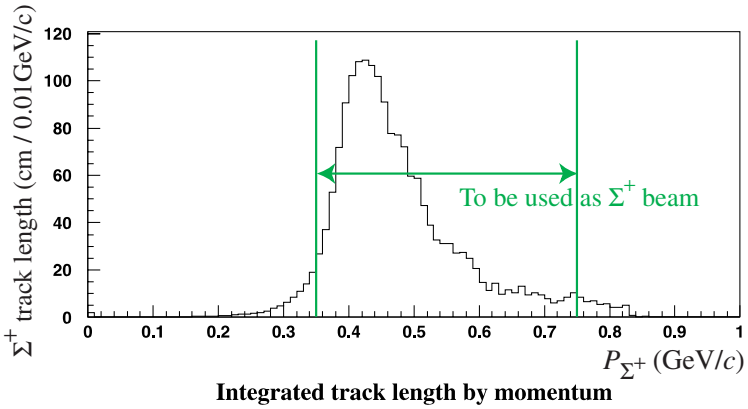

Fig. 13. Momentum distribution of a Σ^+ beam.

$\Delta\theta_\Sigma$ should be defined by l_Σ. We found that the envelope of the $\Delta\theta_\Sigma$ vs l_Σ distribution for simulated $p(\pi^+, K^+)\Sigma^+$ events could be finely fitted by the function $f(l_\Sigma) = a/l_\Sigma + b$. Coefficients a and b were obtained by a least-squares fitting that resulted as $a = 0.17$ and $b = 0.02$. The kinematical cut conditions are summarized as follows:

$$1.162 \text{ GeV}/c^2 < M_{\text{miss}} < 1.221 \text{ GeV}/c^2,$$
$$\Delta\theta_\Sigma < \frac{0.17}{l_\Sigma} + 0.02 \text{ rad.}$$

We divided each Σ^+ track by a track element with a length of 0.015 cm, and calculated the momentum of each element from the missing momentum of (π^+, K^+) kinematics together with the energy loss in the target material. The momentum distribution of Σ^+ is shown in Fig. 13. We summed the track lengths within the momentum region between two lines to obtain the total track length of a Σ^+ beam. The analysis efficiency of a Σ^+ beam (ϵ_{beam}) was obtained by dividing the sum of the measured track lengths of the simulated Σ^+ production events by the generated track length. It was calculated to be 0.895 ± 0.006. The sum of the track lengths of surviving Σ^+ beam candidates in the momentum region from 350 MeV/c to 750 MeV/c was calculated to be

649 ± 5 cm for data set 1. By dividing $\epsilon_{\rm sample}$ and $\epsilon_{\rm beam}$, we obtained a track length of $(1.82 \pm 0.04) \times 10^4$ cm for data set 1. The sum of the track lengths of 1007 ± 6 cm for data set 2 was divided by $\epsilon_{\rm sample}$, $\epsilon_{\rm beam}$, and $\epsilon_{\rm itrack}$ to result in a track length of $(3.19 \pm 0.03) \times 10^4$ cm. The error in the track length was estimated from the difference of the measured track lengths and the generated track lengths of the simulated Σ^+ production data. The total track length of the Σ^+ beam ($L_{\rm beam}$) was $(5.01 \pm 0.04) \times 10^4$ cm. The amount of contamination from Σ^+ produced on carbon nuclei was estimated to be 21.5%.

The target density was calculated from the components of the SCIFI block shown in Table 1. The target number density ($\rho_{\rm targ}$) was calculated to be $(5.00 \pm 0.13) \times 10^{22}$ cm^{-3}. The error includes the imperfection of the thickness of the fiber (2%), the uncertainty of the ratio of water in the extra mutual absorber (1%), and the non-uniformity of the thickness of extra mutual absorber (1.4%).

3.4 $\Sigma^+ p$ elastic-scattering events

The visibility cut conditions for $\Sigma^+ p$ scattering events were determined from the scanning recognition efficiencies using simulation events (Fig. 16 (a)). The Σ^+ track length before the scattering vertex (l_Σ) should be the same of Σ^+ beam candidates. Choosing regions where the recognition efficiencies were flat, l_{Σ_S}(length of scattered Σ^+ track) and l_p(track length of recoil proton) were determined according to the following list:

$$
\begin{aligned}
-9.0 \text{ cm} < V_z &< 6.0 \text{ cm}, \\
l_\Sigma &> 0.5 \text{ cm}, \\
l_p &> 0.5 \text{ cm}, \\
0.3 \text{ cm} < l_{\Sigma_S} &< 5.0 \text{ cm}.
\end{aligned}
$$

Table 1

Summary of the components of the SCIFI block.

scintillating fiber core(83.8 vol%)				
material	density(g/cm^3)	C(mol%)	H(mol%)	others(mol%)
CH($\sim$ 100 %)	1.05	50.1	49.9	0
scintillating fiber clad(7.1 vol%)				
$C_5H_8O_2$(100 %)	1.19	33.3	53.3	13.3
extra mutual absorber(9.1 vol%)				
$Ti0_2$(7.3 mol%)	3.84	-	-	100
H_2O(43.3 mol%)	1.0	-	66.7	33.3
$C_5H_8O_2$(49.4 mol%)	1.19	33.3	53.4	13.3

One more visibility condition was required on the events with the scattered Σ^+ decayed into p and π^0. When the angle between a scattered Σ^+ track and a track of a decay product ($\theta_{\Sigma_S-\mathrm{DP}}$) is small in $\Sigma^+ \to p + \pi^0$ mode, scanners sometimes misidentify a scattered Σ^+ track and a recoil proton track. To eliminate this contamination, we set the following cut:

$$\theta_{\Sigma_S-\mathrm{DP}} > 0.2 \text{ rad} \qquad (\text{for } \Sigma^+ \to p + \pi^0 \text{ and } l_{\Sigma_S} < 1.5 \text{ cm}).$$

For the kinematical selection of $\Sigma^+ p$ elastic scattering, we made use of the difference of a recoil proton momentum ($\Delta\vec{p}_p$), that was defined as follows:

$$\Delta\vec{p}_p = \vec{p}_{p\mathrm{meas}} - \vec{p}_{p\mathrm{miss}},$$

where $\vec{p}_{p\mathrm{meas}}$ was calculated from the pointed track length and the direction of the recoil proton, and $\vec{p}_{p\mathrm{miss}}$ was calculated from the incident momentum of Σ^+ and the scattering angle of Σ^+. Each component of $\Delta\vec{p}_p$ was strongly dependent on the length of the scattered Σ^+ track (l_{Σ_S}), as can be seen in Fig. 14. The dependence was estimated from the $\Delta\vec{p}_p$ distribution of the simulated Σ^+p elastic-scattering events. A scatter diagram of the x-component of $\Delta\vec{p}_p$ (Δp_{p_x}) vs. l_{Σ_S} for the simulated Σ^+p elastic scattering events with subsequent $\Sigma^+ \to n + \pi^+$ decay is shown in Fig. 14. The envelope of the each component of the $\Delta\vec{p}_p$ vs. l_{Σ_S} distribution for simulated events of the Σ^+p elastic scattering were fitted by the function of $f(l_{\Sigma_S}) = a/l_{\Sigma_S} + b$. Parameters a and b were derived for 3 components of $\Delta\vec{p}_p$ and for 2 decay modes of Σ^+. In result, 6 sets of parameters were obtained as given in Table 2.

Table 2

Parameter sets for functions describing the envelopes of 3 components of $\Delta\vec{p}_p$ vs. l_{Σ_S}.

decay mode	$\Sigma^+ \to n + \pi^+$		$\Sigma^+ \to p + \pi^0$	
	a (MeV/c/cm)	b (MeV/c)	a (MeV/c/cm)	b (MeV/c)
Δp_{p_x}	0.039	0.063	0.031	0.081
Δp_{p_y}	0.041	0.063	0.047	0.062
Δp_{p_z}	0.040	0.031	0.023	0.057

In order to simplify the cut condition, we used 3 parameters ($\overline{\Delta p_{p_x}}$, $\overline{\Delta p_{p_y}}$, and $\overline{\Delta p_{p_z}}$), which were obtained from each component of $\Delta\vec{p}_p$ divided by the corresponding functions describing the envelopes at each length of the Σ^+ track. In Fig. 15 (a), the $\overline{\Delta p_{p_z}}$ distribution for the simulated elastic Σ^+p scattering events (a sharp peak) and the simulated quasi-free Σ^+p scattering events

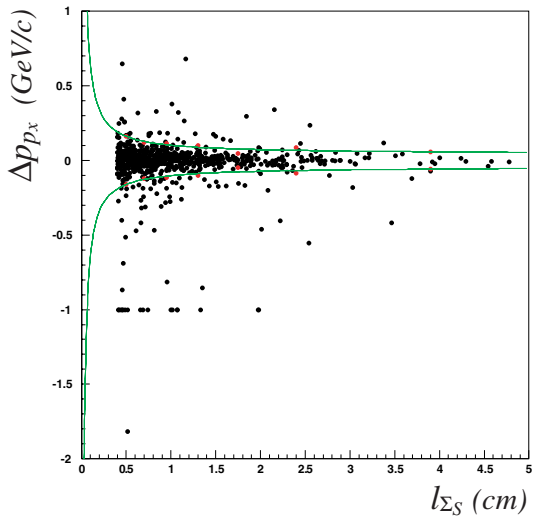

Fig. 14. Scatter diagram of Δp_{p_x} vs. l_{Σ_S} for the simulated $\Sigma^+ p$ elastic scattering events. Two lines show the envelope of the distribution. We used a 2 σ width of Δp_{p_x} in each l_{Σ_S} for the envelope of the distribution.

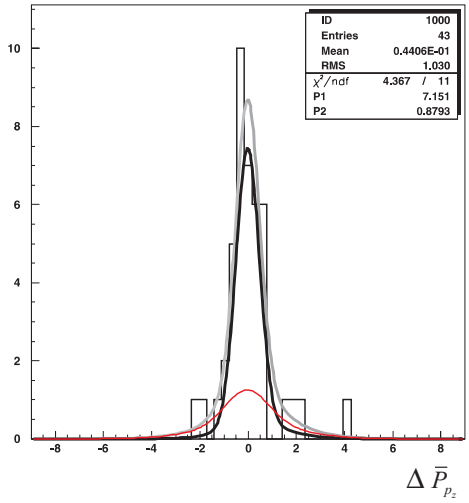

Fig. 15. Distribution of $\overline{\Delta p_{p_z}}$ fitted by the sum of Gaussian curves obtained from the Monte Carlo simulation. The thick black curve represents the distribution for the elastic $\Sigma^+ p$ scattering events, the thin curve represents the distribution for the quasi-elastic $\Sigma^+ p$ scattering events, and the thick gray curve represents the sum of them.

(a broad tail) are shown. Both distributions were fitted by Gaussian curves. From the fitted curves, we estimated the cut efficiency for the elastic scat-

tering events and the contamination of the quasi-free scattering events. By requiring $|\overline{\Delta p_{p_x}}| < 0.7$, $|\overline{\Delta p_{p_y}}| < 0.8$, and $|\overline{\Delta p_{p_z}}| < 0.7$, the quasi-free events were estimated to be suppressed down to 11.4 % while 66.7 % of the elastic scattering events were estimated to survive. In Fig. 15(b), $\overline{\Delta p_{p_z}}$ distribution for the real data are fitted by a sum of the Gaussian curves for the simulated elastic scatterings events and the simulated quasi-free scattering events. The fitting was performed employing the log likelihood method, which produced more stable fitting results than by employing the χ^2 minimization method. From the fitting results, the amount of the background was estimated to be $20.3 \pm 10.7\%$. The error was estimated from the error matrix of the fitting parameters and the fluctuation of fitting result by changing the number of bins of the histogram. We estimated the angular distribution of the background from the distribution of the C-type events rejected by the kinematical conditions for selecting the $\Sigma^+ p$ elastic scattering events. The scattering angle in the center of mass system was obtained from the incident momentum of the Σ^+, the recoil momentum of the proton, and the angle between the incident Σ^+ track and the recoil proton track. From the pointing results of the simulated events, the accuracy of $\cos\theta_{\rm CM}$ was estimated to be 0.14. The analyzing efficiencies (ϵ) for $\Sigma^+ p$ elastic scattering events were estimated from the simulation data (Fig. 16). We have four sets of analyzing efficiency because we have 2 sets of data and 2 decay modes. In table 3, the yields, efficiencies, amount of background, and differential cross sections are summarized. The statistical errors on the yields correspond to the 63.8% probability for the Poisson distribution.

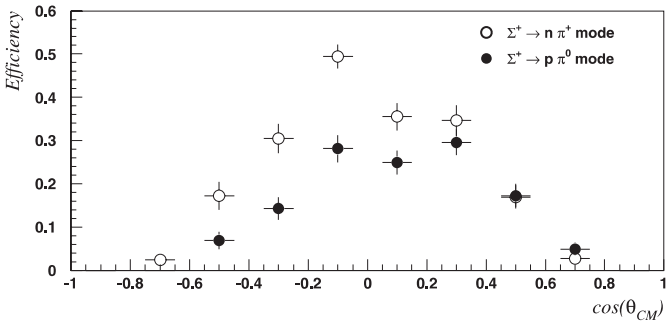

Fig. 16. Angular distribution of the analyzing efficiencies (surviving ratios) of $\Sigma^+ p$ elastic scattering events calculated from simulation data for data set 1. The open circles are for the $\Sigma^+ \to n\pi^+$ decay mode and the closed circles are for the $\Sigma^+ \to p\pi^0$ decay mode. The efficiencies for data set 2 are different by $\epsilon_{\rm itrack}$.

4 Result and discussion

A total of 31 events were identified as $\Sigma^+ p$ elastic scattering. The number of events was roughly 3-times larger than the number of scattering events in the KEK-PS E251 experiment [12]. They were in the momentum region of $350 < p_{\Sigma^+} < 750$ MeV/c and in the angular region of $-0.8 < \cos\theta_{\rm CM} < 0.8$. We estimated the statistical errors from the statistics of the survived real data and also from the statistics of the simulation data. Since the number of the survived events was small, its statistical errors dominated the whole error. The systematical errors contained the contribution of the Σ^+ track length, the target density, and the background subtraction. The error from the background subtraction dominated the systematical errors in all of the angular ranges, as can be seen in the Table 3. The differential cross sections were calculated from

$$\frac{d\sigma}{d\Omega} = \frac{N_{\rm scat}}{L_{\rm beam} \cdot \rho_{\rm targ} \cdot \epsilon \cdot d\Omega}. \tag{1}$$

The differential cross sections for $\Sigma^+ p$ elastic scattering are shown together with the results from the E251 experiment in Fig. 17. The theoretically pre-

dicted differential cross sections from both the Nijmegen group (Fig. 17(a)), [19][20] and from the Kyoto-Niigata group (Fig. 17(b)) [21] at a Σ^+ momentum of 450 MeV/c are also shown in the figure. It is noted that the peak in the most forward region ($\cos\theta > 0.9$) does not appear in the RGM predictions because they do not contain the Coulomb interference. Although both the NSC97 and RGM models predict angular dependence of positive gradient with $\cos\theta$, the RGM predictions show larger values then the NSC97 predictions. The experimental data seem to favor the RGM predictions. The momentum dependence of the Σ^+p elastic scattering cross sections are shown in Fig. 18. The experimental data are integrated in the angular region of $-0.8 < \cos\theta < 0.8$, which are $74.8^{+29.8}_{-22.5}$ mb ($350 < p_{\Sigma^+} < 450$ MeV/c), $26.0^{+24.3}_{15.4}$ mb ($450 < p_{\Sigma^+} < 550$ MeV/c), and $51.7^{+52.2}_{-26.4}$ mb ($550 < p_{\Sigma^+} < 750$ MeV/c). The errors contain statistical and systematical ones. The theoretical predictions integrated in the above region are also shown in the figure. Here again, the experimental data seem to favor the RGM predictions.

5 Summary

The hyperon-nucleon scattering experiment KEK-PS E289 was carried out at the K2 beam line. The differential cross section for Σ^+p elastic scattering was measured with a scintillating fiber active target. The target consisted of 2×10^5 scintillating fibers with cross sections of 300×300 μm^2, and had a fiducial volume of $10 \times 10 \times 20$ cm^3. The photon images from the scintillating fibers were viewed by 2 chains of image intensifying tubes. The target served as a production target for the Σ^+ via $p(\pi^+, K^+)\Sigma^+$ reaction, and also as a scattering target. The information concerning the tracks of charged particles

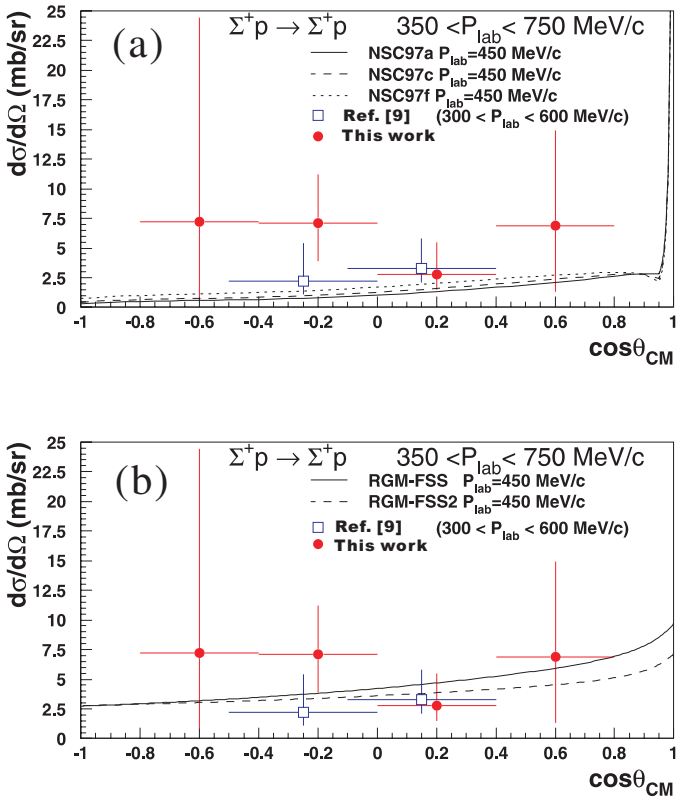

Fig. 17. Differential cross section for $\Sigma^+ p$ elastic scattering. The closed circles show our result and the open squares show the previous result from the KEK-E251 experiment [12]. Theoretical predictions for $p_{\rm lab} = 450$ MeV/c by the NSC97 models (without Coulomb interference) are shown in (a) and the predictions by the RGM models are shown in (b).

relevant to an event was recorded as CCD image data. In 420 hours of beam time, a π^+ beam of 1.64 MeV/c was bombarded on to the target to result in 1.3×10^6 (π^+, K^+) events. Image data of 6.8×10^5 (π^+, K^+) events were eye-scanned for categorization from the track topologies. Consequently, 2.6×10^5 events were categorized as Σ^+ production candidates and 9361 events were categorized as $\Sigma^+ p$ scattering candidates. After requiring kinematical and visibility conditions, 31 events were identified as $\Sigma^+ p$ elastic scattering. They were in the momentum region of $350 < p_{\Sigma^+} < 750$ MeV/c and in the angular region of $-0.8 < \cos\theta_{\rm CM} < 0.8$. The differential cross section was compared

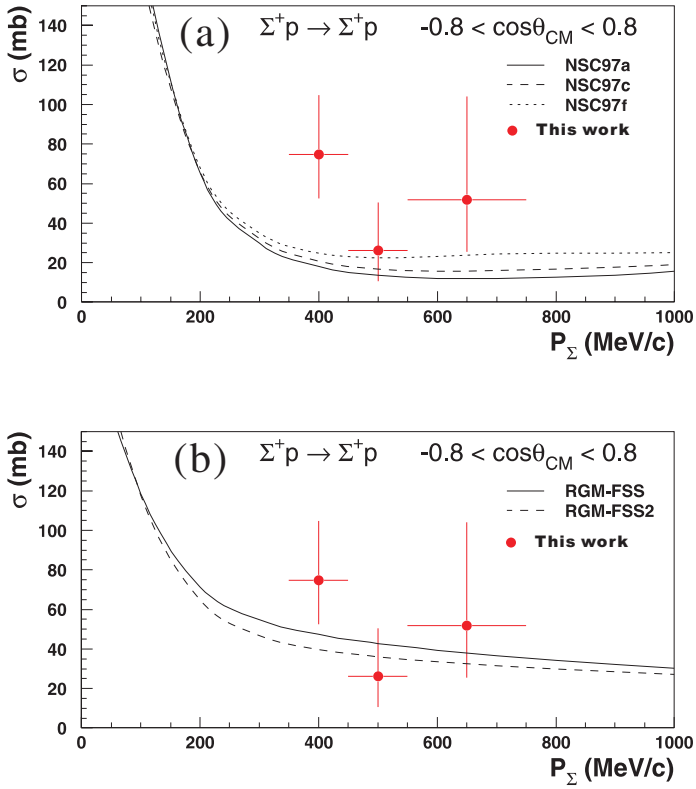

Fig. 18. Integrated differential cross section for Σ^+p elastic scattering. The closed circles show our result and the open squares show the previous result from the KEK-E251 experiment [12]. Theoretical predictions integrated in the same angular region as the experimental data by (a) the NSC97 models and (b) the RGM models are also shown.

to the previous experimental data from KEK-PS E251. They were in agreement within the errors. The differential cross sections and the integrated cross sections were compared to theoretical calculations from both the Nijmegen group (NSC97a, c, and f) and from the Kyoto-Niigata group(RGM-FSS and RGM-fss2) at a Σ^+ momentum of 450 MeV/c. Our results more favored the predictions by the RGM models than those by the NSC97 models.

6 Acknowledgements

We are thankful to the KEK-PS supporting staffs for their effort to maintain the conditions of the accelerators and beam lines throughout our experiments. We would also like to express our gratitude to Profs. H. Sugawara, S. Yamada, K. Nakamura, Y. Yoshimura, and J. Chiba for their support to our experiment and analysis. We owe the theoretical calculations for the $\Sigma^+ p$ elastic cross sections to theoretical physicists. We appreciate Dr. S. Ishikawa, Dr. M.C.M. Rentmeester, and Dr. Th. A. Rijken, for the Nijmegen model calculations. We are thankful to Dr. Y. Fujiwara for the Kyoto-Niigata model calculations. This work was partially supported by a Grants-in-Aid for Scientific Research No. 06640425 of Japan Ministry of Education, Science and Culture. Two (H.K and Y.K) of the collaborators were supported by JSPS Research Fellowships for Young Scientists on this experiment.

References

[1] M.M. Nagels, Th.A. Rijken, J.J. de Swart, Phys. Rev. D 12 (1975) 744;
M.M. Nagels, Th.A. Rijken, J.J. de Swart, Phys. Rev. D 15 (1977) 2547;
M.M. Nagels, Th.A. Rijken, J.J. de Swart, Phys. Rev. D 20 (1979) 1633

[2] M.M. Nagels, Th.A. Rijken, J.J. de Swart, Phys. Rev. D 17 (1978) 768;
V.G.J. Stokes, R.A.M. Klomp, C.P.F. Terheggen, J.J. de Swart, Phys. Rev. C 49 (1994) 2950;
P.M.M. Maessen, Th.A. Rijken, and J.J. de.Swart, Phys. Rev. C 40 (1989) 2226;
Th.A. Rijken, V.G.J. Stokes, and Y. Yamamoto, Phys. Rev. C 59 (1999) 21;
V.G.J. Stokes and Th.A. Rijken, Phys. Rev. C 59 (1999) 3009.

[3] S. Ishikawa, M. Tanifuji, Y. Iseri, and Y. Yamamoto, Phys. Rev. C 69 (2004) 034001.

[4] B. Holtzenkamp, K. Holinde, J. Speth, Nucl. Phys. A 500 (1989) 485; A. Reuber, K. Holinde, J. Speth, Nucl. Phys. A 570 (1994) 573.

[5] C. Nakamoto, Y. Suzuki, Y. Fujiwara, Prog. Theor. Phys. 94 (1995) 65;
Y. Fujiwara, C. Nakamoto, Y. Suzuki, Prog. Theor. Phys. 94 (1995) 215, 353;
Y. Fujiwara, C. Nakamoto, Y. Suzuki, Phys. Rev. Lett. 76 (1996) 2242;
Y. Fujiwara, C. Nakamoto, Y. Suzuki, Phys. Rev. C 54 (1996) 2180;
Y. Fujiwara, K. Miyagawa, M. Kohno, and Y. Suzuki, Phys. Rev. C 70 (2004) 024001;
Y. Fujiwara, C. Nakamoto, Y. Suzuki, M. Kohno, and K. Miyagawa, nucl-th/0404070, to be submitted to Prog. Theor. Phys. Suppl.

[6] M. Oka, K. Yazaki, in : W.Weise (Ed.) Quarks and Nuclei, World Scientific, 1984, p.489;
K. Yazaki in T. Yamazaki, K. Nakai, K. Nagamine (Eds.), Perspectives of Meson Science,Elsevier, 1992, p.795.

[7] U. Straub, Z.Y. Zhang, K. Bräuer, A. Faessler, S.B. Khadkikar, G. Lübeck, Nucl. Phys. A 483 (1988) 686, A 508 (1990) 385c.

[8] R.A. Arndt et al., Phys. Rev. D 28 (1983) 97.

[9] SAID online program, R.A. Arndt et al. `http://gwdac.phys.gwu.edu/`.

[10] Nijmegen NN-OnLine, M.C.M. Rentmeester, `http://nn-online.org/`.

[11] H.G. Dosch et al., Phys. Lett. B 21 (1966) 236, 587;
G. Alexander et al., Phys. Rev. 173 (1968) 1452;
B. Sechi-Zorn et al. Phys. Rev. 175 (1968) 1735;
G.R. Charlton et al. Phys. Lett. B 32 (1970) 720;
F. Eisele et al., Phys. Lett. B 37 (1971) 204;

J.A. Kadyk et al., Nucl. Phys. B 27 (1971) 13;
J.M. Hauptmann et al., Nucl. Phys. B 125 (1977) 29.

[12] J.K. Ahn et al., Nucl. Phys. A 648 (2000) 263.

[13] J.K. Ahn et al., Nucl. Inst. Meth. A 457 (2001) 137.

[14] Y. Kondo et al., Nucl. Phys. A 676 (2000) 371.

[15] M. Ishino et al., Nucl. Inst. Meth. A 457 (2001) 581.

[16] `http://www.netlib.org/dierckx/`.

[17] R. Brun et al., GEANT: SIMULATION PROGRAM FOR PARTICLE PHYSICS EXPERIMENTS. USER GUIDE AND REFERENCE MANUAL. CERN-DD-78-2-REV, CERN-DD-78-2, Jul 1978. 76pp. Revised Version.;
GEANT: Detector Description and Simulation Tool, CERN Program Library Long Writeup W5013.

[18] D.J. Candlin et al., Nucl. Phys. B 226 (1983) 1-28.

[19] S. Ishikawa, private communications.

[20] M.C.M. Rentmeester and Th.A. Rijken, private communications.

[21] Y. Fujiwara, private communications. QMPACK online program,
`http://ruby2.scphys.kyoto-u.ac.jp/person/fujiwara/QMPACK/index.html`

Table 3

Yields of $\Sigma^+ p$ elastic scattering, efficiencies, backgrounds, and differential cross sections for two data sets and two decay modes.

$\cos\theta_{\rm CM}$			-0.8∼-0.4	-0.4∼ 0	0∼0.4	0.4 ∼ 0.8
Set 1	$n\pi^+$	$N_{\rm scat}$	$2^{+2.6}_{-1.3}$	$1^{+2.3}_{-0.8}$	$3^{+2.9}_{-1.6}$	$0^{+1.8}_{-0.0}$
		$\epsilon(\%)$	9.33 ± 1.69	40.4 ± 2.2	35.1 ± 2.3	10.1 ± 1.6
		$N_{\rm scat}/\epsilon$	$21.4^{+28.5}_{-14.4}$	$2.47^{+5.68}_{-2.05}$	$8.54^{+8.32}_{-4.68}$	$0.00^{+18.2}_{-0.00}$
	$p\pi^0$	$N_{\rm scat}$	$0^{+1.8}_{-0.0}$	$2^{+2.6}_{-1.3}$	$2^{+2.6}_{-1.3}$	$0^{+1.8}_{-0.0}$
		$\epsilon(\%)$	3.27 ± 0.99	20.2 ± 2.1	27.1 ± 2.0	10.9 ± 1.5
		$N_{\rm scat}/\epsilon$	$0.00^{+56.2}_{-0.00}$	$9.89^{+13.07}_{-6.47}$	$7.38^{+9.73}_{-4.79}$	$0.00^{+16.9}_{-0.00}$
Set 2	$n\pi^+$	$N_{\rm scat}$	$2^{+2.6}_{-1.3}$	$7^{+3.8}_{-2.6}$	$2^{+2.6}_{-1.3}$	$4^{+3.2}_{-2.9}$
		$\epsilon(\%)$	8.27 ± 1.50	35.8 ± 2.0	31.1 ± 2.1	8.96 ± 1.42
		$N_{\rm scat}/\epsilon$	$24.2^{+32.2}_{-16.2}$	$19.5^{+10.6}_{-7.28}$	$6.43^{+8.49}_{-4.17}$	$44.7^{+36.0}_{-33.3}$
	$p\pi^0$	$N_{\rm scat}$	$1^{+2.3}_{-0.8}$	$4^{+3.2}_{-2.9}$	$0^{+1.8}_{-0.0}$	$1^{+2.3}_{-0.8}$
		$\epsilon(\%)$	2.90 ± 0.88	17.9 ± 1.85	24.0 ± 1.8	9.65 ± 1.37
		$N_{\rm scat}/\epsilon$	$34.5^{+80.0}_{-30.4}$	$22.3^{+17.8}_{-16.4}$	$0.00^{+7.65}_{-0.00}$	$10.4^{+23.8}_{-8.69}$
summed $N_{\rm scat}/\epsilon$			$80.1^{+106.8}_{-37.3}$	$54.2^{+25.1}_{-19.2}$	$22.4^{+17.2}_{-7.9}$	$55.0^{+49.8}_{-34.4}$
$N_{\rm BG}/\epsilon$			34.7 ± 14.3	9.4 ± 4.0	4.8 ± 1.8	11.4 ± 6.2
(summed $N_{scat} - N_{\rm BG})/\epsilon$			$45.4^{+107.7}_{-40.0}$	$44.8^{+25.4}_{-19.6}$	$17.6^{+17.3}_{-8.09}$	$43.6^{+50.2}_{-34.9}$
$\frac{d\sigma}{d\Omega} \pm stat. \pm syst.$ (mb/sr)			$7.2^{+17.0}_{-5.9} \pm 2.6$	$7.1^{+4.0}_{-3.1} \pm 0.8$	$2.8^{+2.7}_{-1.3} \pm 0.3$	$6.9^{+7.9}_{-5.5} \pm 1.0$